JOURNAL OF GEOPHYSICAL RESEARCH, VOL. 117, C04035, doi:10.1029/2011JC007697, 2012

Interannual North Equatorial Countercurrent variability and its relation to tropical Atlantic climate modes

Verena Hormann,[1,2] Rick Lumpkin,[2] and Gregory R. Foltz[2]

Received 19 October 2011; revised 13 March 2012; accepted 15 March 2012; published 28 April 2012.

[1] A synthesis product of the surface geostrophic circulation is used to quantify the interannual variability of the wind-driven North Equatorial Countercurrent (NECC). The first mode of a complex empirical orthogonal function (CEOF) decomposition of zonal geostrophic velocity in the NECC region reveals pronounced latitudinal displacements in addition to variations in current strength. While north-south migrations of the NECC are mainly captured by the real pattern, the imaginary pattern accounts for variations in its strength. Associated with these spatial patterns is prevailing propagation toward the northwest that is most pronounced northward of the mean NECC position (~6°N). There is evidence that the zonal propagation characteristics are consistent with long Rossby waves forced in the northeastern tropical Atlantic. The relationship between interannual NECC variations and the tropical Atlantic climate modes is investigated through regression and composite analyses. Sea surface temperature and wind stress patterns resembling the meridional and zonal modes are found for the CEOF regression. Composite analysis further shows consistent patterns for warm phases of the meridional mode and cold phases of the zonal mode; the response of the NECC to a positive meridional and negative zonal mode event may be viewed as a northward shift of its core and a current strengthening, respectively. These results support a link between the two dominant tropical Atlantic climate modes and show that the relation between interannual NECC variability and the meridional and zonal modes can primarily be regarded as a response to changes in the wind field.

Citation: Hormann, V., R. Lumpkin, and G. R. Foltz (2012), Interannual North Equatorial Countercurrent variability and its relation to tropical Atlantic climate modes, *J. Geophys. Res.*, *117*, C04035, doi:10.1029/2011JC007697.

1. Introduction

[2] The Atlantic North Equatorial Countercurrent (NECC) is a major component of the climate system and flows generally eastward between about 3°–10°N (Figure 1), bounded by the westward North Equatorial Current (NEC) and the northern branch of the South Equatorial Current (nSEC). There is evidence for a northern branch or two-core structure of the NECC which is at least a semi-persistent feature [e.g., *Polonsky and Artamonov*, 1997; *Stramma et al.*, 2005, 2008; *Urbano et al.*, 2006, 2008; *Artamonov*, 2006]. The position of the NECC coincides with the Atlantic's warmest waters (cf. Figure 1: mean sea surface temperature (SST) in its western source region, 3°–10°N, 50°–40°W, is 27.8°C) [*Enfield and Mayer*, 1997] and it has been identified as a source for oxygen-rich water supplied to the oxygen minimum zone of the tropical North Atlantic [*Stramma et al.*, 2005, 2008]. Moreover the NECC is a main pathway for the upper-ocean return flow of the meridional overturning circulation, connecting the North Brazil Current (NBC) to the circulation in the interior tropical North Atlantic [*Fratantoni et al.*, 2000; *Jochum and Malanotte-Rizzoli*, 2001].

[3] The NECC is characterized as a wind-driven, geostrophic current and varies profoundly on seasonal timescales, closely tied to the migration of the Intertropical Convergence Zone (ITCZ). Its seasonal cycle has been extensively studied since the early 1980s [e.g., *Garzoli and Katz*, 1983; *Richardson and Reverdin*, 1987; *Garzoli and Richardson*, 1989; *Garzoli*, 1992; *Korotaev and Chepurin*, 1992; *Polonsky and Artamonov*, 1997; *Yang and Joyce*, 2006; *Artamonov*, 2006], but less is known about the interannual variability of the NECC. Both *Garzoli and Richardson* [1989] and *Didden and Schott* [1992] observed year-to-year differences of the seasonal NECC fluctuations, and *Katz* [1993] noted considerable variations on interannual timescales following El Niño events in the Pacific. In the western equatorial Atlantic, *Arnault et al.* [1999] observed a clear year-to-year variability in the northern NECC region. Significant anomalies in NECC position and strength during certain years were also found by *Fonseca et al.* [2004], without showing any consistent pattern over their investigation period.

---

[1] Cooperative Institute for Marine and Atmospheric Studies, University of Miami, Miami, Florida, USA.

[2] NOAA/Atlantic Oceanographic and Meteorological Laboratory, Miami, Florida, USA.

Corresponding Author: V. Hormann, Cooperative Institute for Marine and Atmospheric Studies, University of Miami, 4301 Rickenbacker Cswy., Miami, FL 33149, USA. (verena.hormann@noaa.gov)

0148-0227/12/2011JC007697

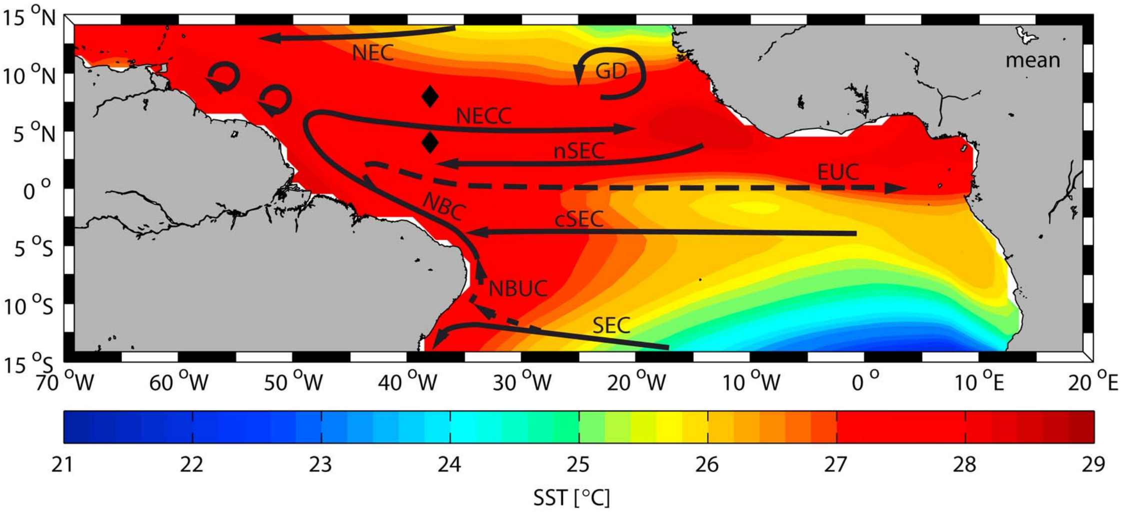

Figure 1. Schematic of surface (solid) and thermocline (dashed) tropical Atlantic currents [after *Brandt et al.*, 2011], including the North Equatorial Countercurrent (NECC), North Equatorial Current (NEC), South Equatorial Current (SEC) along with its northern and central branches (nSEC, cSEC), North Brazil Current and Undercurrent (NBC, NBUC), Equatorial Undercurrent (EUC), as well as the cyclonic circulation around the Guinea Dome (GD), superimposed on the mean SST for the period October 1992 to December 2009. Diamonds mark PIRATA buoys at 4°N and 8°N, 38°W.

[4] In the Pacific, *Johnston and Merrifield* [2000] revealed that interannual variations of the western NECC are related to the El Niño Southern Oscillation (ENSO), and *Zhang and Busalacchi* [1999] even proposed a possible link between off-equatorial warm anomalies propagating along the NECC path and the onset of the 1997–98 El Niño. A simple ENSO cycle of upper-ocean currents in the tropical Pacific, including the NECC, was estimated by *Johnson et al.* [2002] from direct measurements. Interannual variability of simulated upper-ocean currents in the equatorial Atlantic was also found in association with the zonal mode [*Góes and Wainer*, 2003; *Hormann and Brandt*, 2007], one of the two dominant modes of interannual-to-decadal climate fluctuations in the tropical Atlantic and counterpart to the Pacific ENSO [e.g., *Chang et al.*, 2006, and references therein]. SST anomalies associated with this mode are most pronounced in the eastern equatorial cold tongue region during boreal summer, and the underlying feedback is thought to be the dynamical Bjerknes mechanism [e.g., *Zebiak*, 1993; *Keenlyside and Latif*, 2007].

[5] During boreal spring, conditions in the tropical Atlantic are favorable for the development of an anomalous inter-hemispheric SST gradient, giving rise to the meridional mode. The wind-evaporation-SST (WES) feedback mechanism appears to be an important driver of this thermodynamic mode [e.g., *Chang et al.*, 1997]. In addition, along with the North Atlantic Oscillation (NAO), ENSO has been proposed to be a factor of external influence [e.g., *Czaja et al.*, 2002; *Enfield and Mayer*, 1997]. Both the meridional mode and NECC are believed to be mainly wind-driven, and positive WES feedback is thought to be strongest in the western Atlantic warm pool region [e.g., *Chang et al.*, 1997] where the NECC originates. The most notable climate impacts of these two dominant modes in the tropical Atlantic are the variability of rainfall over northeast Brazil and the coastal regions surrounding the Gulf of Guinea, as well as fluctuations in rainfall and dustiness in sub-Saharan Africa (Sahel) [e.g., *Chang et al.*, 2006, and references therein].

[6] Despite differences in seasonality and governing mechanisms, the coupled spatial patterns associated with the meridional and zonal modes bear some resemblance, motivating *Servain et al.* [1999] to propose a link between them. A recent study by *Foltz and McPhaden* [2010] revealed that the interaction between the meridional and zonal modes is mediated by directly wind-forced equatorial Kelvin waves and the delayed negative feedback from western boundary reflections of wind-forced Rossby waves.

[7] More generally, Rossby waves are critical for the transient adjustment of ocean circulation to changes in large-scale atmospheric forcing. Using satellite altimetry, *Chelton and Schlax* [1996] showed that Rossby waves are present in much of the world ocean, with typical amplitudes of 10 cm or smaller and wavelengths of more than 500 km. That study further revealed discrepancies between observed and theoretical Rossby wave speeds, most pronounced outside of the tropical band from 10°S to 10°N.

[8] Rossby waves were also found to play an important role in the dynamics of the NECC as first noted by *Garzoli and Katz* [1983], who determined that both local wind stress curl and Rossby waves from the eastern basin contribute to its seasonal variations. On the other hand, *Yang and Joyce* [2006] hypothesized that wind stress fluctuations along the equator are more important than local wind stress curl in driving the seasonal cycle of the NECC. This hypothesis is based on altimeter observations showing the NECC's seasonal transport variability to be dominated by sea surface height (SSH) changes on the southern flank which is partially located in the equatorial waveguide; a sensitivity experiment with a reduced-gravity model forced by a wind stress field with zero curl showed that most of the seasonal transport variability is retained [*Yang and Joyce*, 2006]. To explain the observed interannual NECC variability, *Katz* [1993] applied

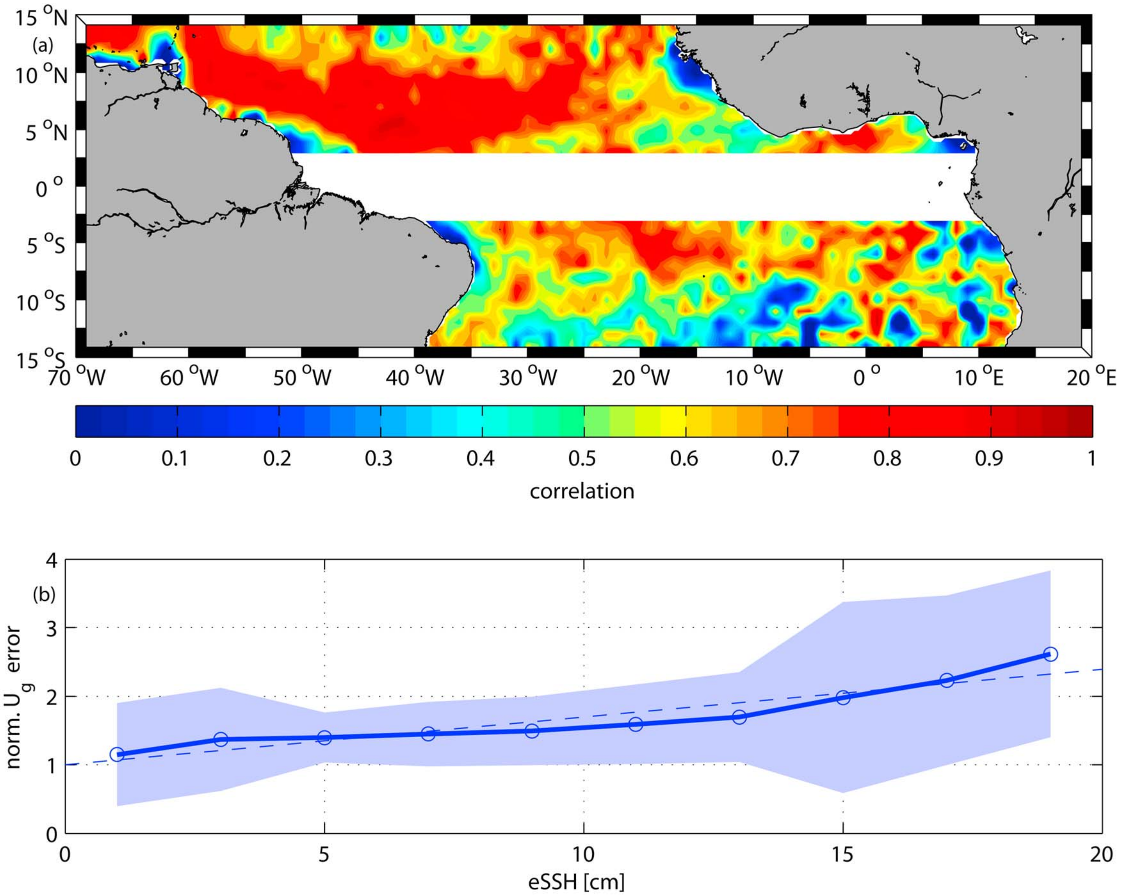

Figure 2. (a) Spatial correlation between Ekman-removed drifter velocity anomalies and altimetry-derived geostrophic velocity anomalies. (b) Normalized error in zonal geostrophic velocity (similar results for meridional velocity) as a function of *eSSH* in all 2° × 2° bins in the tropical Atlantic. Values have been averaged in *eSSH* bins (solid line), with shading indicating the standard deviation. A least squares fit of a straight line (dashed) and estimate of the spatially varying velocity error in the limit *eSSH* → 0 is used to calculate the time- and space-varying error in geostrophic velocity in the synthesis product.

an unbounded reduced-gravity model presuming that these fluctuations should be traceable back to changes in the surface wind field on the same timescale. This simple model was incapable of reproducing the observed variability, which he attributed to the assumptions of the model, the inadequacy of the wind field forcing the model, or both.

[9] The first objective of this study is to quantify interannual NECC variations (Section 3.1) based on a synthesis product of the surface geostrophic circulation (Section 2.1) for the period October 1992 to December 2009, starting when satellite SSH observations became obtainable and complementary data (Section 2.2) are also available. These results are then applied to an investigation of the interannual NECC variability in relation to the coupled climate modes in the tropical Atlantic (Section 3.2). Discussion and conclusions are provided in Section 4.

2. Data

2.1. Synthesis Product

[10] Mean zonal (U) and meridional (V) currents including their seasonal variations were calculated in 1° bins from satellite-tracked surface drifter velocities [*Lumpkin and Garraffo*, 2005; *Lumpkin and Garzoli*, 2005]. Eddy currents (u', v') were derived with respect to the mean currents as $u' = u - U$, $v' = v - V$, where u (v) is the total zonal (meridional) speed of a drifter. By removing the Ekman component from the eddy currents, these observations can be compared to geostrophic velocity anomalies calculated from altimetry. We use here the updated, delayed-time Archiving, Validation and Interpretation of Satellite Oceanographic data (AVISO) gridded SSH product starting in October 1992 [*Le Traon et al.*, 1998], with geostrophic currents in the equatorial band computed after *Lagerloef et al.* [1999]. Ekman components were derived from National Centers for Environmental Prediction (NCEP) operational winds using the *Ralph and Niiler* [1999] model, with updated coefficients from *Niiler* [2001].

[11] The correlation between the resulting Ekman-removed velocity anomalies and geostrophic velocity anomalies was significant in the region of the NECC: the mean correlation coefficient in the region 3°–10°N, 40°–15°W was $cc = 0.70$ with a spatial standard deviation of 0.12 (Figure 2a). This correlation allows the altimetry and drifter data to be synthesized using the methodology of *Niiler et al.* [2003]. The synthesis produces weekly snapshots of geostrophic

near-surface currents at 1/3° resolution, adjusts the drifter time-mean current field to account for aliased sampling of interannual anomalies, and adjusts the variance of the altimetry-derived currents to match the time-mean eddy kinetic energy of the Ekman-removed drifter velocity anomalies where the two are correlated.

[12] Error bars on the resulting zonal and meridional currents can be estimated from the *a posteriori* (time-independent) root-mean square (RMS) differences between the geostrophic velocity synthesis product and the Ekman-removed drifter velocities. These error estimates implicitly include errors in the Ekman model, as this is an additional source of discrepancy between the two sets of velocities. Differences between the altimetry currents and the drifter-derived currents vary spatially as described by spatial variations in the drifter/altimetry correlation (cf. Figure 2a), and temporally due to variations in altimeter coverage, the latter reflected in the formal error bar of SSH (*eSSH*) provided by the AVISO product. To derive the time- and space-varying error, we sought to combine the RMS differences with *eSSH* and their relationship was determined as follows: Mean normalized errors (RMS error divided by the error in the limit $eSSH \rightarrow 0$) were calculated in 2° × 2° bins and plotted as a function of *eSSH*. The result increased approximately linearly, from 1 at $eSSH = 0$ (by definition) to ∼1.65 at $eSSH = 10$ cm to ∼2.5 at $eSSH = 20$ cm (Figure 2b). A least squares linear fit to this relationship was used in all bins and interpolated to the 1/3° values of the synthesis product to derive the time- and space-varying error bars (cf. Figure 3b).

[13] The end time of the synthesis product was chosen to be December 2009 due to availability of complementary data (cf. Section 2.2).

2.2. Complementary Data

[14] Surface winds are provided by the cross-calibrated multiplatform (CCMP) ocean surface wind vector L3.5a pentad first-look analyses (ftp://podaac-ftp.jpl.nasa.gov/allData/ccmp/L3.5a/pentad/flk) [*Atlas et al.*, 2011]. This data set is globally available from July 1987 to December 2009, with a horizontal resolution of 0.25° × 0.25° and a temporal resolution of five days. For the purpose of this study, we first interpolated the data onto the time vector of the synthesis product and mapped the tropical Atlantic surface winds onto a 1° × 1° horizontal grid by applying a Gaussian interpolation scheme to close remaining gaps. Corresponding zonal and meridional wind stresses as well as wind stress curl were derived using version 3.0 of the Coupled Ocean-atmosphere Response Experiment (COARE) bulk algorithm [*Fairall et al.*, 2003].

[15] We also use the NOAA optimum interpolation SST V2 data set provided by the NOAA/OAR/ESRL PSD, Boulder, Colorado, USA, from their web site at http://www.esrl.noaa.gov/psd/ [*Reynolds et al.*, 2002]. Data are available on a 1° × 1° global grid as weekly means from October 1981 onward and were interpolated onto the time vector of the synthesis product.

[16] The surface data sets are complemented by subsurface temperature and salinity data from two Prediction and Research Moored Array in the Tropical Atlantic (PIRATA) Buoys located at 4°N and 8°N, 38°W (cf. Figure 1) (http://www.pmel.noaa.gov/pirata/) [*Bourlès et al.*, 2008]. We use 5-day averages of temperatures in the upper 180 m from March 2000 (4°N) and February 1998 (8°N), respectively, to December 2009, when data coverage is sufficient (Table 1). Surface gaps were first padded with the NOAA SST data set (RMS differences between the two time series: 0.21°C at 4°N and 0.27°C at 8°N), and a Delaunay-triangulation interpolation method [*Barber et al.*, 1996] was used to fill subsurface gaps with a regular 20 m depth spacing. The data were also mapped onto the time vector of the synthesis product. For further mooring calculations, we estimated corresponding seasonal salinity cycles for both sites using available buoy data along with mean temperature-salinity relations from the World Ocean Atlas 2009 [*Locarnini et al.*, 2010; *Antonov et al.*, 2010] to fill salinity gaps.

[17] In the following, we refer to seasonal anomalies as fluctuations relative to the respective harmonic seasonal cycle (i.e., subtracting the first two annual harmonics), with interannual anomalies additionally 275-day low-pass filtered.

3. Results

[18] First, we present a description of the NECC and its variability, focusing on interannual timescales. The relation of the interannual NECC variability to the tropical Atlantic climate modes is then examined in the second part of this section.

3.1. NECC Variability

[19] In agreement with earlier studies [e.g., *Garzoli and Katz*, 1983; *Richardson and Reverdin*, 1987; *Lumpkin and Garzoli*, 2005], the surface current synthesis product shows an eastward geostrophic current band associated with the mean NECC confined mainly to 3°–10°N (Figure 3a). Except for the southeastern part, this region coincides with a positive mean wind stress curl indicating proximity to the ITCZ [e.g., *Garzoli and Richardson*, 1989; *Garzoli*, 1992; *Fonseca et al.*, 2004]. In the west, the NECC is primarily supplied by the NBC retroflection and also fed by northern hemisphere water from the NEC [e.g., *Arhan et al.*, 1998; *Bourlès et al.*, 1999]. Supplied by westward South Equatorial Current branches, the northward-increasing NBC is clearly visible along the Brazilian shelf north of about 12°S. The NECC extends across the entire basin toward the African coast where it bifurcates into the cyclonic Guinea Dome to the north and the coastal Guinea Current to the southeast.

[20] A time series of the NECC core position (defined as the latitude of maximum eastward velocity) further illustrates that this current can mainly be found in the latitude band 3°–10°N (Figure 3b). There are pronounced latitudinal displacements during October 1992 to December 2009, with a mean NECC position at about 6°N. The prevailing eastward velocity (mean, with standard deviation: 0.20 ± 0.12 m/s), superimposed on a strong seasonal cycle, with maxima (minima) generally occurring during boreal summer and winter (spring), is highlighted by a time series of the NECC at its mean position (Figure 3c). Note that there is not a consistent relationship between the time series of NECC core position and strength.

[21] The NECC is well known for its large annual fluctuations in phase with the annual variation of the wind stress curl, including a reversal in the western basin during boreal spring [*Garzoli and Katz*, 1983]. Our harmonic analysis

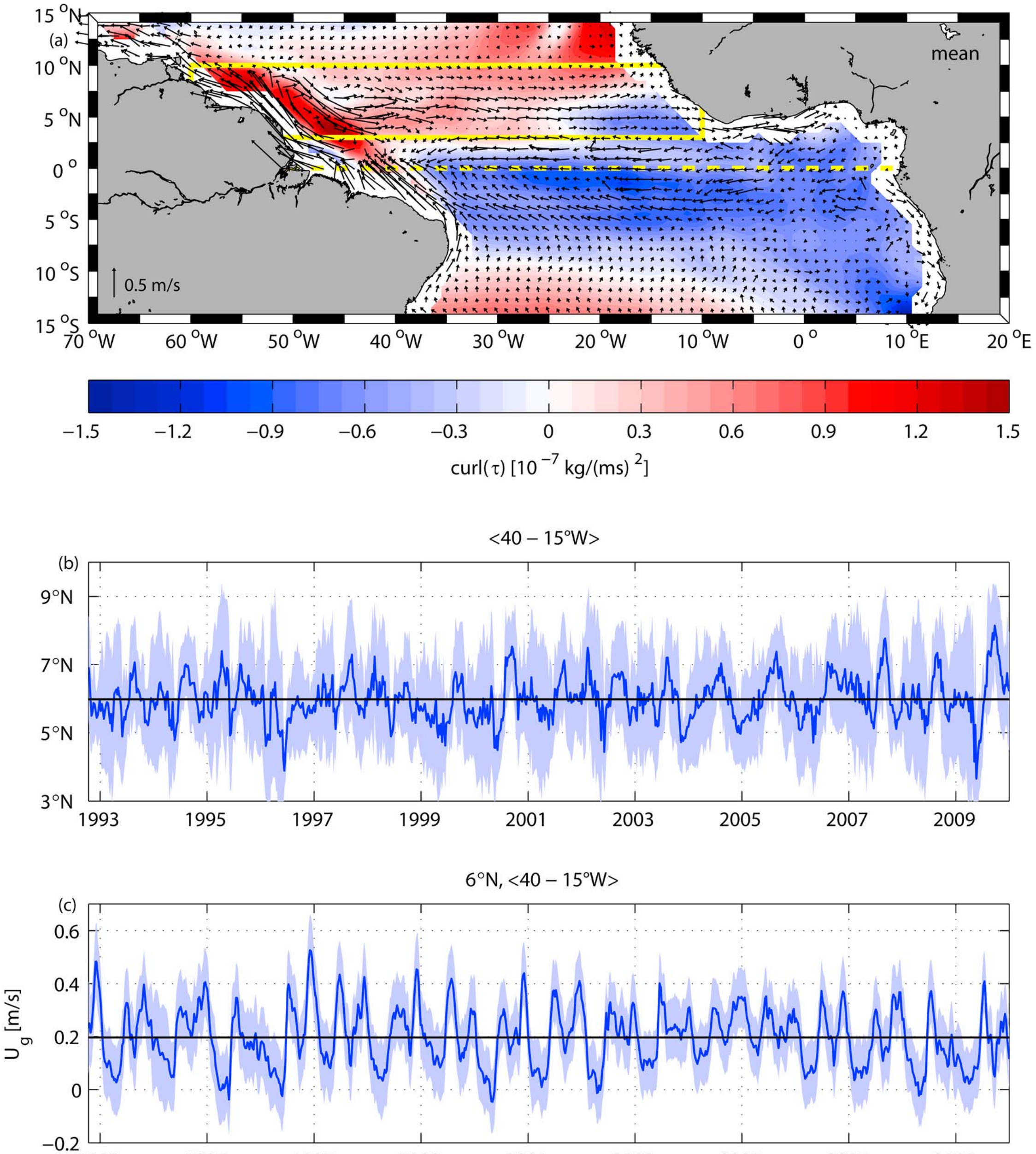

Figure 3. (a) Mean surface geostrophic circulation of the tropical Atlantic during October 1992 to December 2009 (each third grid point only), superimposed on the corresponding mean wind stress curl. Yellow box marks NECC region and yellow dashed line indicates the equator. Time series of (b) NECC core position, with longitudinal standard deviation (shaded), and (c) zonal geostrophic velocity at 6°N, averaged between 40°–15°W, with error estimate (shaded). Means in Figures 3b and 3c are marked by black lines.

Table 1. Percentage of Available Temperature Data at Each Depth Level for the 38°W-PIRATA buoys at 4°N (Mar 2000 to Dec 2009) and 8°N (Feb 1998 to Dec 2009)

	Z (m)								
	1	20	40	60	80	100	120	140	180
4°N, 38°W	71.8%	79.3%	59.1%	95.7%	90.3%	93.5%	75.5%	86.4%	96.0%
8°N, 38°W	76.2%	76.7%	75.3%	99.9%	89.4%	95.4%	82.1%	100.0%	100.0%

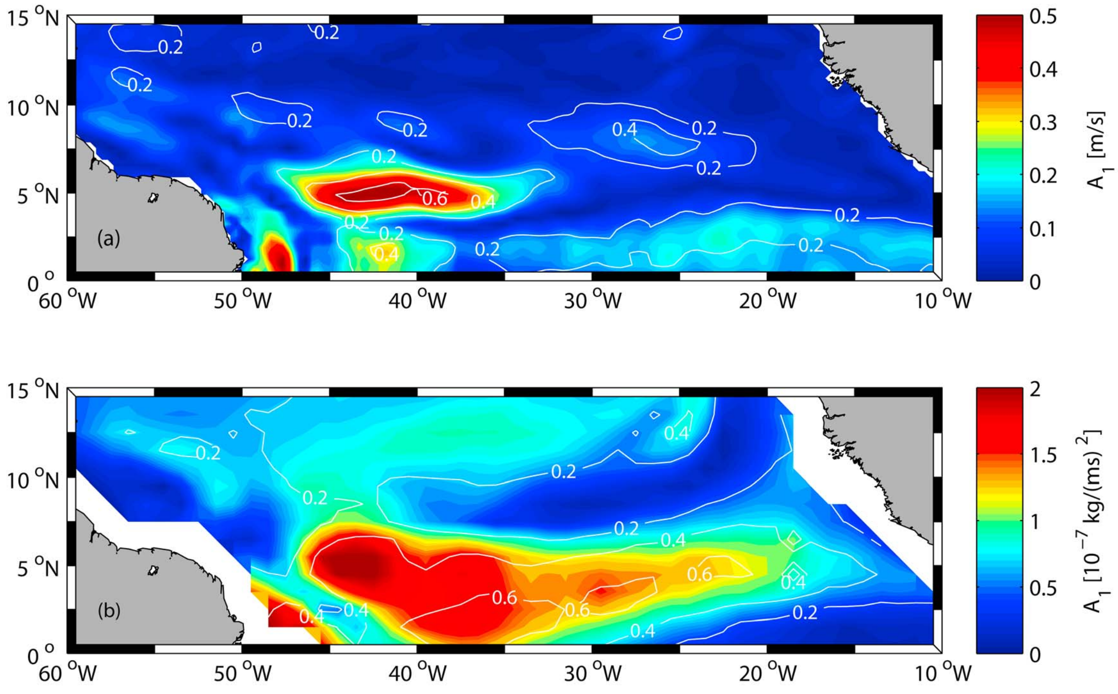

Figure 4. Annual harmonic amplitude of (a) zonal geostrophic velocity and (b) wind stress curl, with superimposed explained variances, in the northern tropical Atlantic.

supports these results, showing large annual amplitudes and high explained variances for both zonal geostrophic velocity and wind stress curl particularly in the western NECC region (Figure 4), with corresponding semi-annual components comparatively small (not shown).

[22] The NECC not only reveals pronounced fluctuations on seasonal timescales but also on longer ones [e.g., *Garzoli and Richardson*, 1989; *Katz*, 1993] which can be seen in latitude-time diagrams (Figure 5). Most obvious are year-to-year variations in current core strength (e.g., mid-90s) and position (about 6 ± 2°N) as well as overall current width. To the south the NECC is well separated from the westward nSEC, while eastward velocities generally prevail to the north and are strongest around the mean NECC position. Note that there might also be indications of the recently rediscovered northern NECC branch or two-core structure [*Urbano et al.*, 2006] as for instance in the second half of 1996.

[23] A variance-conserving power spectrum of seasonal zonal geostrophic velocity anomalies at 6°N (Figure 6) indicates enhanced energy on interannual timescales, particularly between about 50°–25°W, with additional maxima in the intraseasonal period band. *Richardson and Reverdin* [1987] first noted that energetic fluctuations with periods of a few months are superimposed on the dominant annual variation of the NECC, and a more recent model study by *Jochum and Malanotte-Rizzoli* [2003] showed that the NECC is barotropically unstable, radiating Rossby waves of the first baroclinic mode. However, the focus of this study is on the longer timescales associated with climate fluctuations in the tropical Atlantic.

[24] To describe the NECC variability on interannual timescales, we applied a complex empirical orthogonal function (CEOF) analysis (for details see, e.g., *Barnett* [1983] and *Hormann and Brandt* [2009]) to the corresponding zonal geostrophic velocity anomalies in the NECC region (cf. Figure 3a). As the NECC shows pronounced latitudinal displacements in addition to variations in current strength (cf. Figures 3b, 3c and 5), this technique is more suitable than traditional EOF analysis because it is capable of detecting propagating features in space. The first CEOF mode explains about 26% of the variance (compared to 13% for the second one) and its temporal evolution reveals large undulations in the mid-90s as well as since 2005 (Figure 7a). The real pattern can mainly be described by velocities opposite in sign north and south of about 6°N, with maxima/minima around 35°W (Figure 7b). Anomaly maxima around this mean NECC position and mainly westward of about 30°W are found for the corresponding imaginary pattern, with a transition to velocities of opposite sign at about 7.5°N (Figure 7c). The relative phase between the real and imaginary spatial patterns increases toward the northwest, indicating prevailing northwestward propagation that is most pronounced northward of about 6°N (Figure 7d). For example during 2001/2002, the NECC appears to be shifted southward in boreal summer 2001 (negative real pattern) followed by a current strengthening in boreal fall (dominant imaginary pattern) and a displacement to the northwest in boreal winter (positive real pattern). In other words, north–south migrations of the NECC are mainly captured by the real pattern, while the imaginary pattern accounts for variations in its strength.

[25] The Radon transform provides a means to elucidate the zonal propagation characteristics of the northwestward signal found particularly to the north of the mean NECC position (for details see, e.g., *Deans* [1983] and *Maharaj et al.* [2009]). Following equation 5 of *Hormann and Brandt* [2009], we first derived interannual SSH anomalies

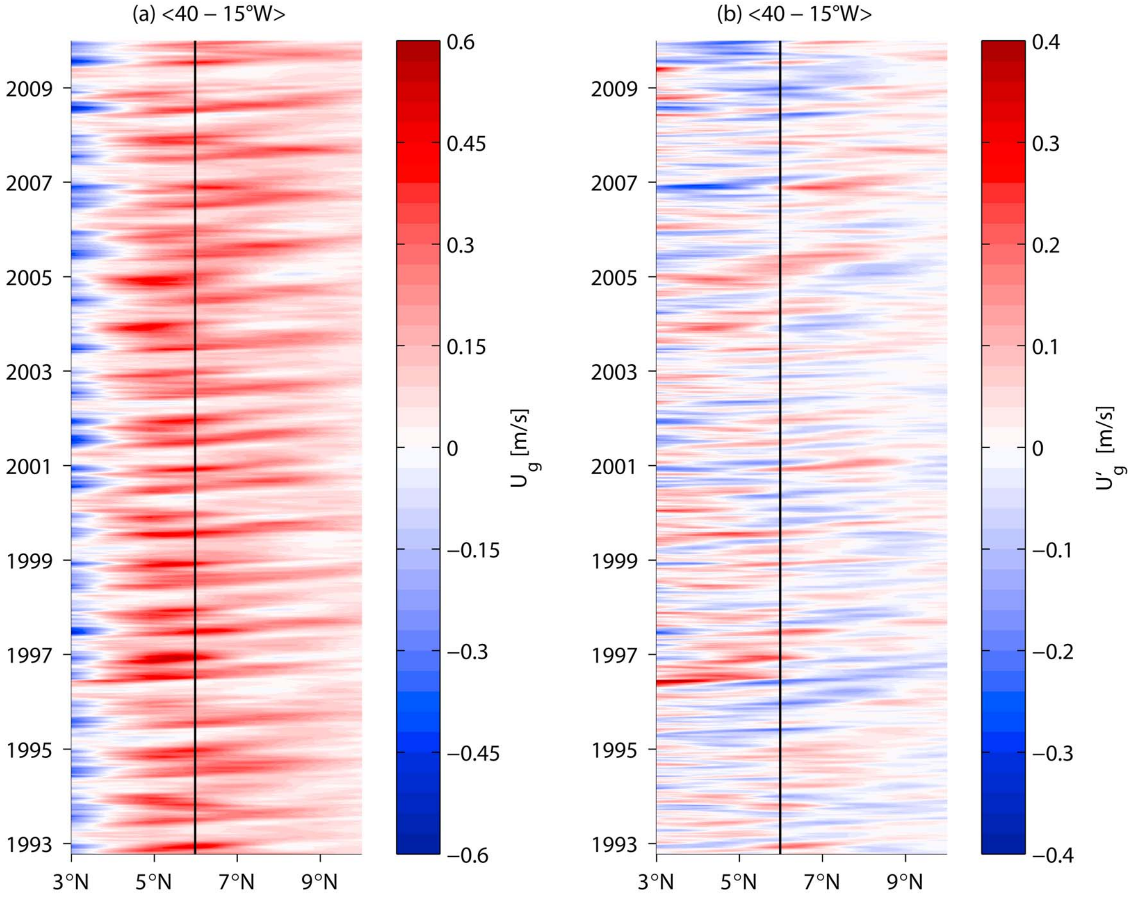

Figure 5. Latitude-time diagram of (a) zonal geostrophic velocity and (b) corresponding seasonal anomalies (i.e., first two annual harmonics subtracted) averaged between 40°–50°W. Black line marks mean NECC position.

associated with the first CEOF mode by linear regression (cf. Figure 8c). To objectively estimate the propagation speed of the predominant signal, one needs to find the angle for which the energy of the Radon transform is maximum and then compute the corresponding speed using simple trigonometry (Figures 8a and 8b). Taking up an approach by *Maharaj et al.* [2009], we assessed the uncertainties associated with the resulting propagation speeds (e.g., $c_{rt} = -0.29$ m/s at 8°N) in the following manner: Gaussian white noise on the interval $[-1\ 1]$, with zero mean, is added to the Radon transform. The transform is then inverted to produce a corresponding longitude-time section that is used to compute the Radon transform again. A thousand such simulations were run to estimate 95% confidence intervals (Figure 8b).

[26] The first baroclinic mode Rossby wave speed can be derived from the long-wave approximation using the Rossby

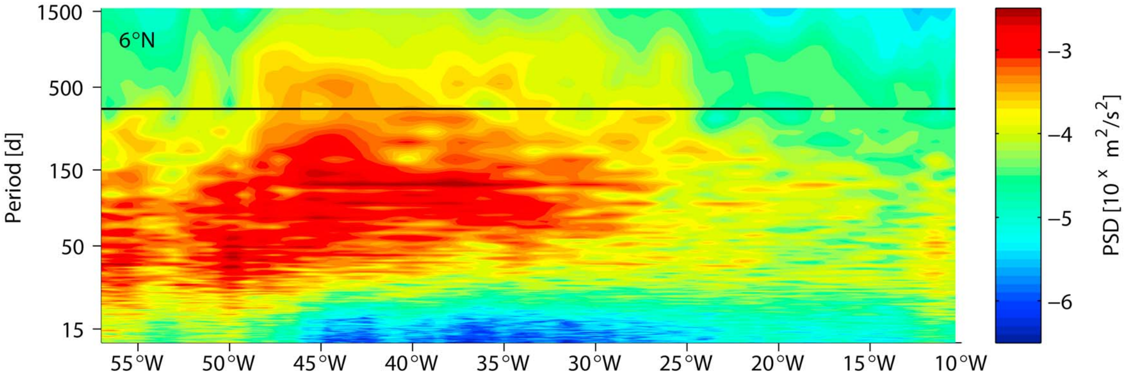

Figure 6. Variance-conserving power spectrum of seasonal zonal geostrophic velocity anomalies (i.e., first two annual harmonics subtracted) at 6°N. Black line marks 365-day period.

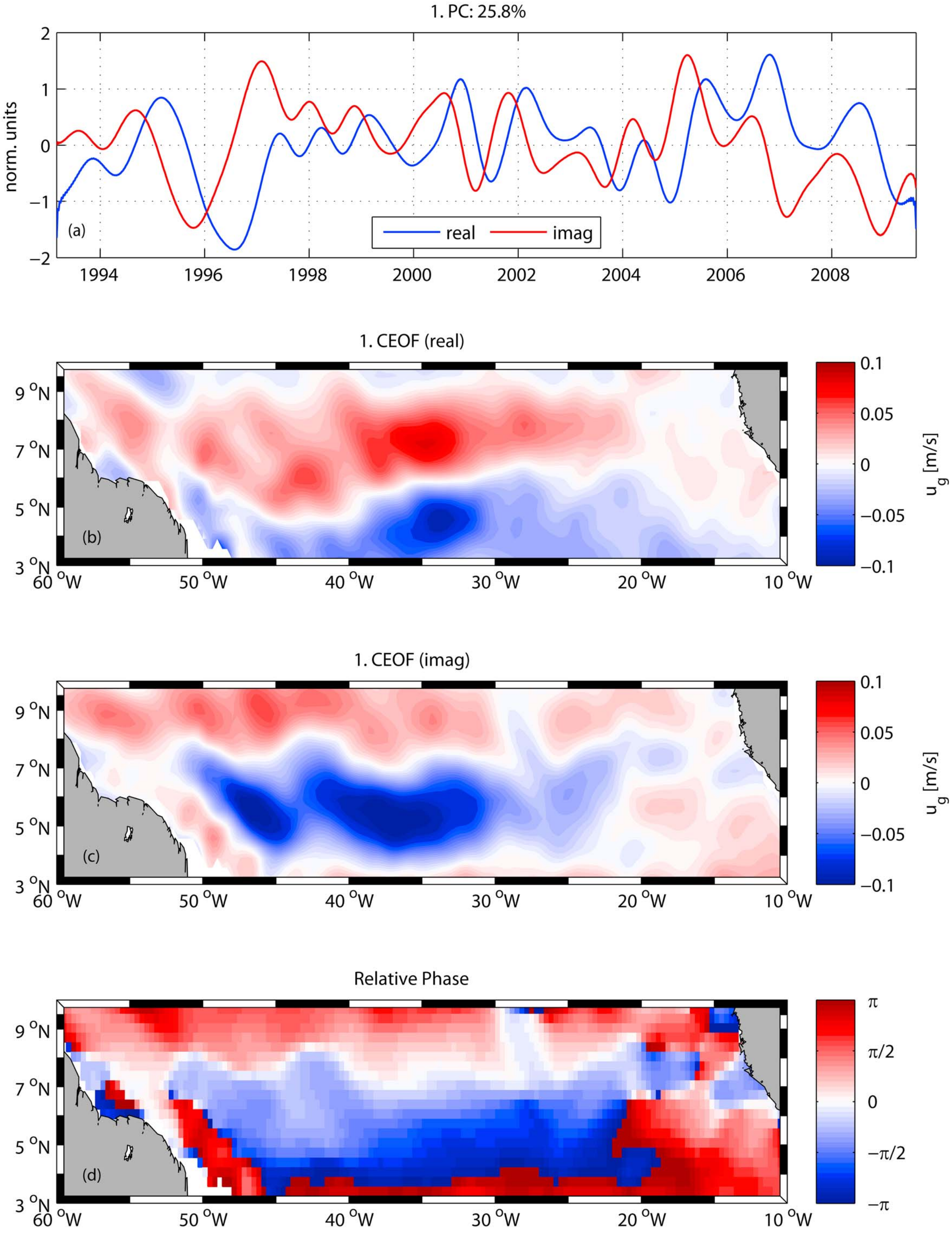

1. PC: 25.8%

1. CEOF (real)

1. CEOF (imag)

Relative Phase

Figure 7. First CEOF mode of interannual zonal geostrophic velocity anomalies in the NECC region: (a) real (blue) and imaginary (red) temporal components; (b) real and (c) imaginary spatial patterns; (d) relative phase associated with the spatial pattern.

radius of deformation by *Chelton et al.* [1998], with uncertainty estimates based on the longitudinal standard deviation of the Rossby radius. A comparison of our Radon-transform-based propagation speeds with these Rossby wave speeds (Figure 8b) shows largely statistical agreement between the two estimates south of 8.5°N, strongly suggesting the presence of Rossby waves in the latitude band of the NECC. North of this latitude, there are indications of another change in sign of the CEOF real-pattern velocities (cf. Figure 7b) as well as of secondary maxima in the energy angular density of the Radon transform at small angles (cf. Figure 8a). The latter are associated with eastward propagation speeds and might be indicative of short Rossby waves.

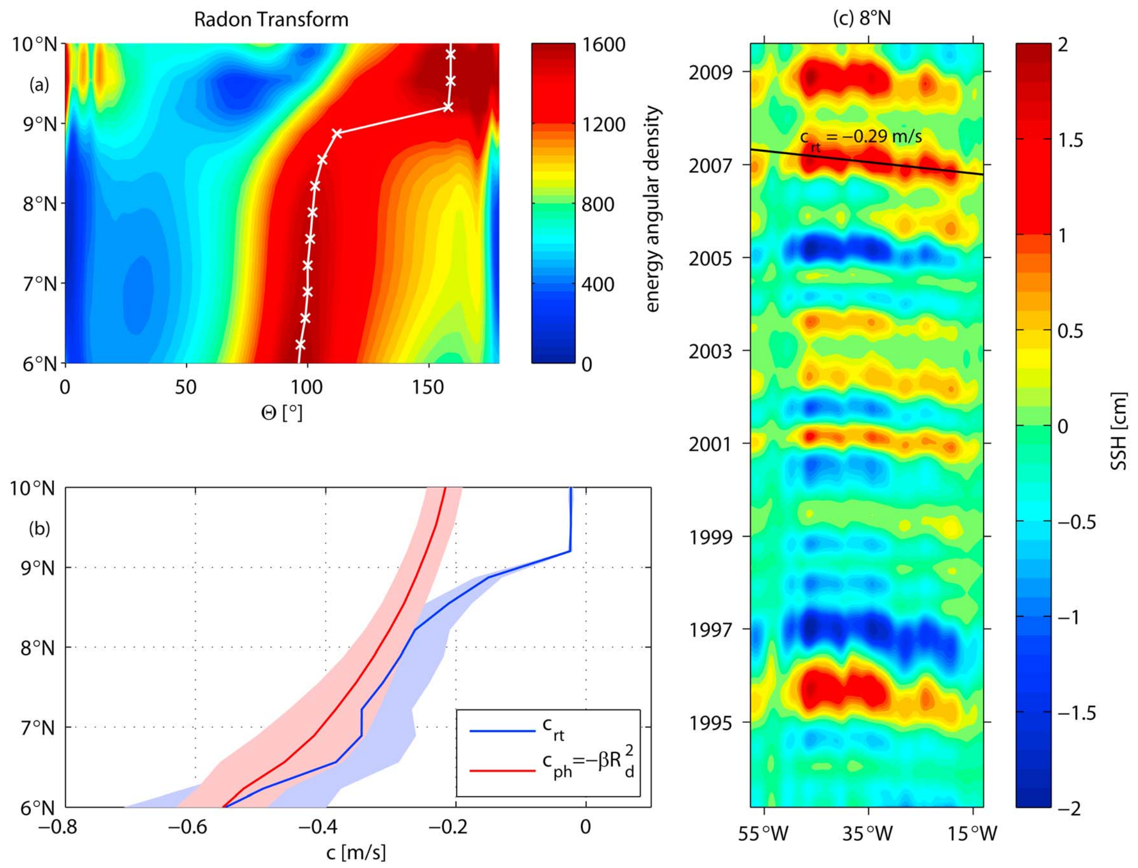

Figure 8. Interannual SSH anomalies associated with the first CEOF mode: (a) energy angular density of the Radon transform (arbitrary units), with white line indicating the angle of maximum energy angular density; (b) Rossby wave speeds calculated from the Radon transform (c_{rt}; blue) and long-wave approximation ($c_{ph} = -\beta R_d^2$, where $\beta = df/dy$ is the latitudinal variation of the Coriolis parameter and R_d is the Rossby radius of deformation; red), with uncertainty estimates (shaded); (c) longitude-time diagram at 8°N, with marked westward phase speed obtained from the Radon transform.

3.2. Relation to Tropical Atlantic Climate Modes

[27] Climate fluctuations in the tropical Atlantic on interannual-to-decadal timescales are dominated by the meridional and zonal modes [e.g., *Chang et al.*, 2006, and references therein], with interannual SST variability largest in the tropical North Atlantic and the eastern equatorial/tropical South Atlantic (Figure 9a). Following *Servain* [1991], we define the meridional mode as the difference between interannual SST anomalies averaged over 5°–25°N, 60°–20°W and 20°S–5°N, 30°W–10°E and the zonal mode as the average over the ATL3 region 3°S–3°N, 20°W–0° [*Zebiak*, 1993]. The resulting time series are significantly (95% level) anti-correlated, with a correlation coefficient of $cc = -0.53$. This is also reflected in extreme years of opposite sign like 1997, 2005, and 2008 (Figure 9b); the 2005 events in particular have been discussed in great detail [*Foltz and McPhaden*, 2006; *Hormann and Brandt*, 2009; *Marin et al.*, 2009]. Given that the coupled spatial patterns associated with the two dominant tropical Atlantic climate modes bear some resemblance, *Servain et al.* [1999] first proposed a link between them and *Foltz and McPhaden* [2010] have shown that this interaction is mediated by wind-forced equatorial waves and their boundary reflections. Thus, the result finding particularly extreme events of opposite sign in the same year further supports a link between the meridional and zonal modes.

[28] Similar to *Servain et al.* [1999], we examined the relation between these modes and interannual ITCZ position anomalies (here based on a zero-wind stress-curl criterion), finding a good correlation between the meridional mode and anomalous ITCZ positions ($cc = 0.74$) which is not the case for the zonal mode ($cc = -0.22$). Using equatorial thermocline slope anomalies to describe the zonal mode, *Servain et al.* [1999] found both modes to be associated with latitudinal shifts of the ITCZ and proposed that the link between them involves processes much the same as those controlling the seasonal cycle.

[29] The first CEOF mode describing interannual NECC variations can be used to investigate its relationship with SST and wind stress variability in the tropical Atlantic by means of a regression analysis (Figure 10). SST regression coefficients corresponding to the real part of the mode's temporal evolution show prevailing positive (negative) anomalies in the northern (southern) hemisphere (Figure 10a) which bear resemblance to the SST pattern associated with the meridional mode. This modal pattern is also consistent with the corresponding wind stress pattern indicating anomalous

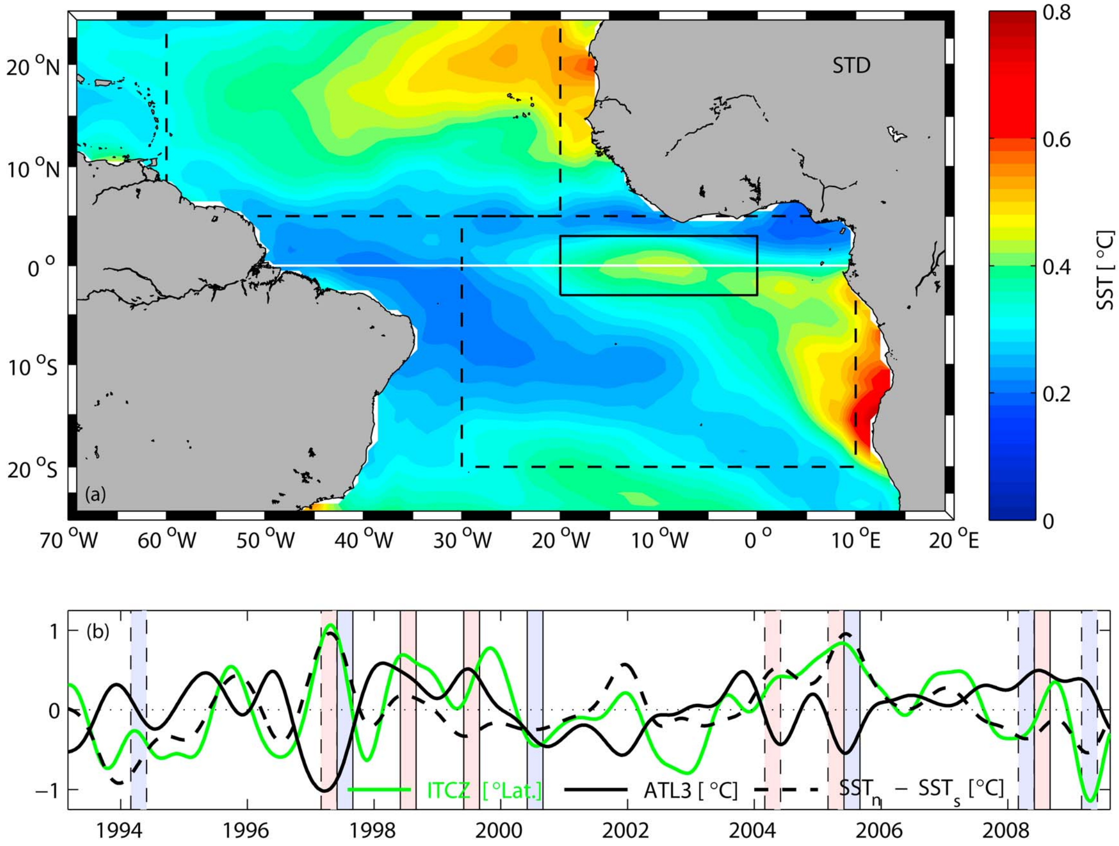

Figure 9. (a) Standard deviation of interannual SST anomalies in the tropical Atlantic. Black lines mark ATL3 region (solid) as well as northern [SST_n] and southern [SST_s] boxes (dashed) used to form the meridional mode index [$SST_n - SST_s$]. White line indicates the equator. (b) ATL3 (black solid) and $SST_n - SST_s$ (black dashed) time series, along with interannual ITCZ position anomalies (green). Shadings are the three warmest (red) and coldest (blue) years during the peak season of the meridional (March–May; black dashed contours) and zonal (June–August; black solid contours) mode, respectively.

winds from the cold to the warm hemisphere. The imaginary pattern, on the other hand, reveals largest SST anomalies in the eastern equatorial as well as southeastern coastal regions and prevailing negative anomalies in the northern hemisphere (Figure 10b). The corresponding wind stress coefficients show a reduction of the equatorial trade winds to the west of the ATL3 region. This pattern strongly indicates a relation between the interannual NECC variability and the zonal mode, typically characterized by anomalous winds in the west and SSTs in the east. Overall, this means that latitudinal shifts of the NECC are associated mainly with the boreal spring meridional mode while variations in its strength are more closely related to the boreal summer zonal mode.

[30] Given that the anomalous wind patterns include in both cases northwestward wind stress anomalies in the western equatorial Atlantic, a possible interaction between the meridional and zonal modes may occur via the mechanism suggested by *Foltz and McPhaden* [2010]. Note also that both the real and imaginary components show correlation with remarkable wind stress fluctuations in the northeastern tropical Atlantic, discussed in Section 4.

[31] To further illustrate the relationship between the interannual variability of the wind-driven NECC and the meridional and zonal modes, we computed composites of interannual zonal geostrophic velocity and wind stress curl anomalies associated with the first CEOF mode for the three warmest and coldest years during the respective peak season of these modes (Figure 11; meridional/zonal mode: boreal spring 1997, 2004, 2005 versus 1994, 2008, 2009/boreal summer 1998, 1999, 2008 versus 1997, 2000, 2005). In boreal spring, the NECC is generally weak or even vanishes in the west and is shifted southward (cf. Figures 3b, 3c and 5a). During meridional-mode warm (cold) events, positive (negative) velocity anomalies are particularly prominent west of about 30°W around the mean NECC position, with wind stress curl anomalies opposite in sign to the north and south of the maximum velocity fluctuations (Figure 11a and 11b). In contrast, the NECC is well established about its mean position in boreal summer (cf. Figures 3b, 3c and 5a). Interannual anomalies are generally weak in the NECC region during zonal-mode warm events (Figure 11d), while the corresponding cold-phase pattern resembles that of the meridional-mode warm phase (Figure 11c). Given the similarity of these patterns to the strong phase of the annual NECC cycle as first shown by *Garzoli and Katz* [1983], the dynamics involved on interannual and seasonal timescales might be alike; this implies, for instance, an anomalous northward shift of the ITCZ during meridional-mode warm and zonal-mode cold events. However, the actual response of the NECC may be different during these events due to its

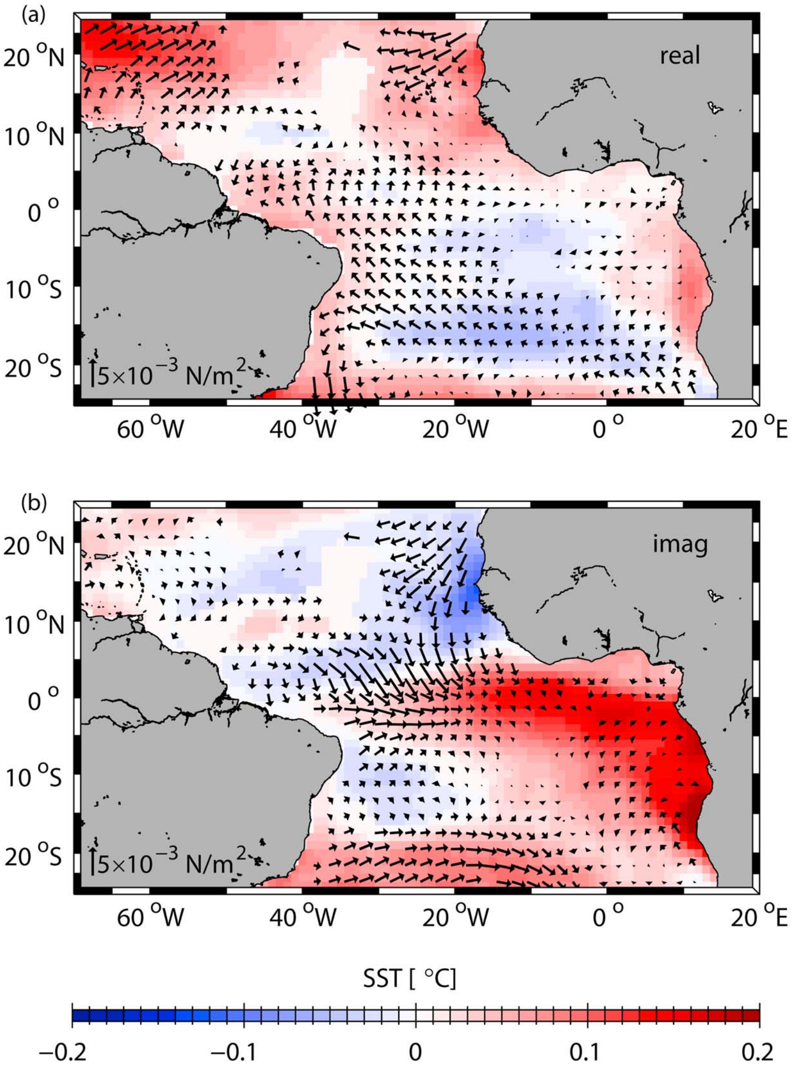

Figure 10. (a) Real and (b) imaginary regression patterns of interannual SST (coloring) as well as zonal and meridional wind stress (vectors; each second grid point only) anomalies onto the temporal component of the first CEOF mode (cf. Figure 7a); values are shown only where significant at 95% level.

pronounced seasonal migrations. For example, positive velocity anomalies associated with meridional-mode warm and zonal-mode cold phases suggest a northward shift of the NECC core in boreal spring, while such anomalies result in a strengthening of the NECC in boreal summer.

[32] The two PIRATA buoys at 38°W within the NECC allow further investigation of interannual changes in the 20°C-isotherm depth and upper-ocean heat content as well as subsurface geostrophic velocity (Figure 12). At both 4°N and 8°N, interannual 20°C-isotherm depth and heat content anomalies are highly correlated with each other (Figures 12a and 12b) but correlation between the two mooring sites is rather low or even insignificant (20°C-isotherm depth: $cc = -0.31$, heat content: $cc = 0.07$). Interannual anomalies associated with the first CEOF mode (not shown) explain about 36(41)% of the 20°C-isotherm depth (heat content) variance at 4°N, while only about 13(10)% of the variance is accounted for at 8°N. The 8°N-time series can principally be described by prevailing negative (positive) anomalies before (since) 2004, whereas the most striking features at 4°N are two distinct anomalies of opposite sign in 2005 and 2008/2009. The 4°N-anomalies are also reflected in corresponding pronounced fluctuations of geostrophic velocities referenced to the synthesis product (Figure 12c), with both these events occurring in extreme years of the tropical Atlantic climate modes (cf. Figure 9b). These velocity fluctuations are also consistent with our CEOF analysis as illustrated by the extreme-event composites suggesting prevailing positive and negative anomalies during 2005 and 2008/2009, respectively (cf. Figure 11).

[33] Based on these observations, we examined the importance of NECC advection for the meridional and zonal modes by performing a simulation of the evolution of a tracer released around 6°N, 38°W [cf. *Maximenko et al.*, 2012]. This simulation utilizes the Lagrangian probability density functions from all available drifters (total zonal and meridional speeds) that were also used in the synthesis product. Using drifter data from all months and years averages over seasonal-to-interannual variations of the NECC; for instance, one would expect that by limiting the Lagrangian simulation

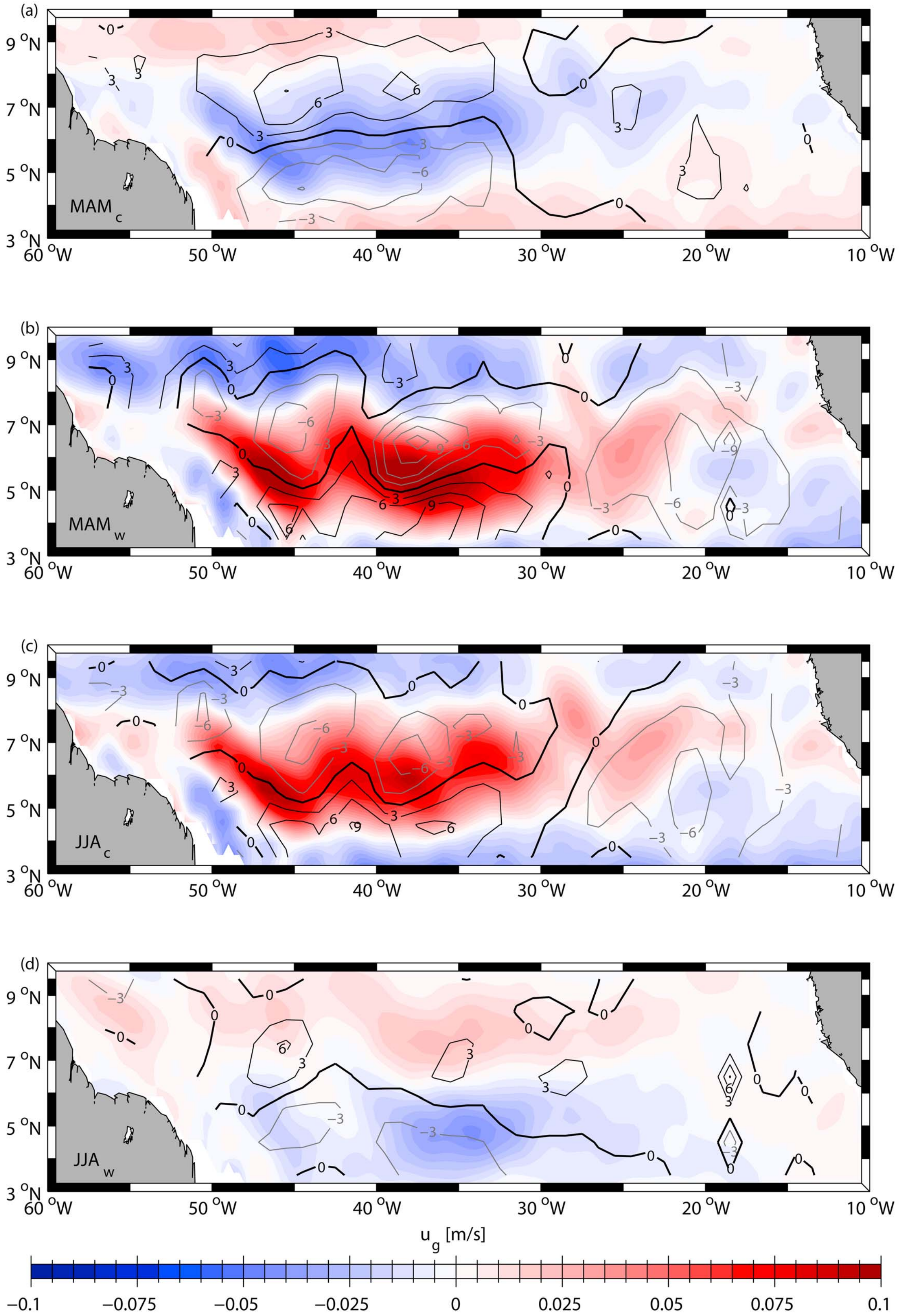

Figure 11. Composites of interannual zonal geostrophic velocity (coloring) and wind stress curl (contours, in intervals of 3×10^{-9} kg/(ms)^2) anomalies associated with the first CEOF mode for the three (b and d) warmest and (a and c) coldest years during the peak season of the meridional (March–May; Figures 11a and 11b) and zonal (June–August; Figures 11c and 11d) mode, respectively (cf. Figure 9b).

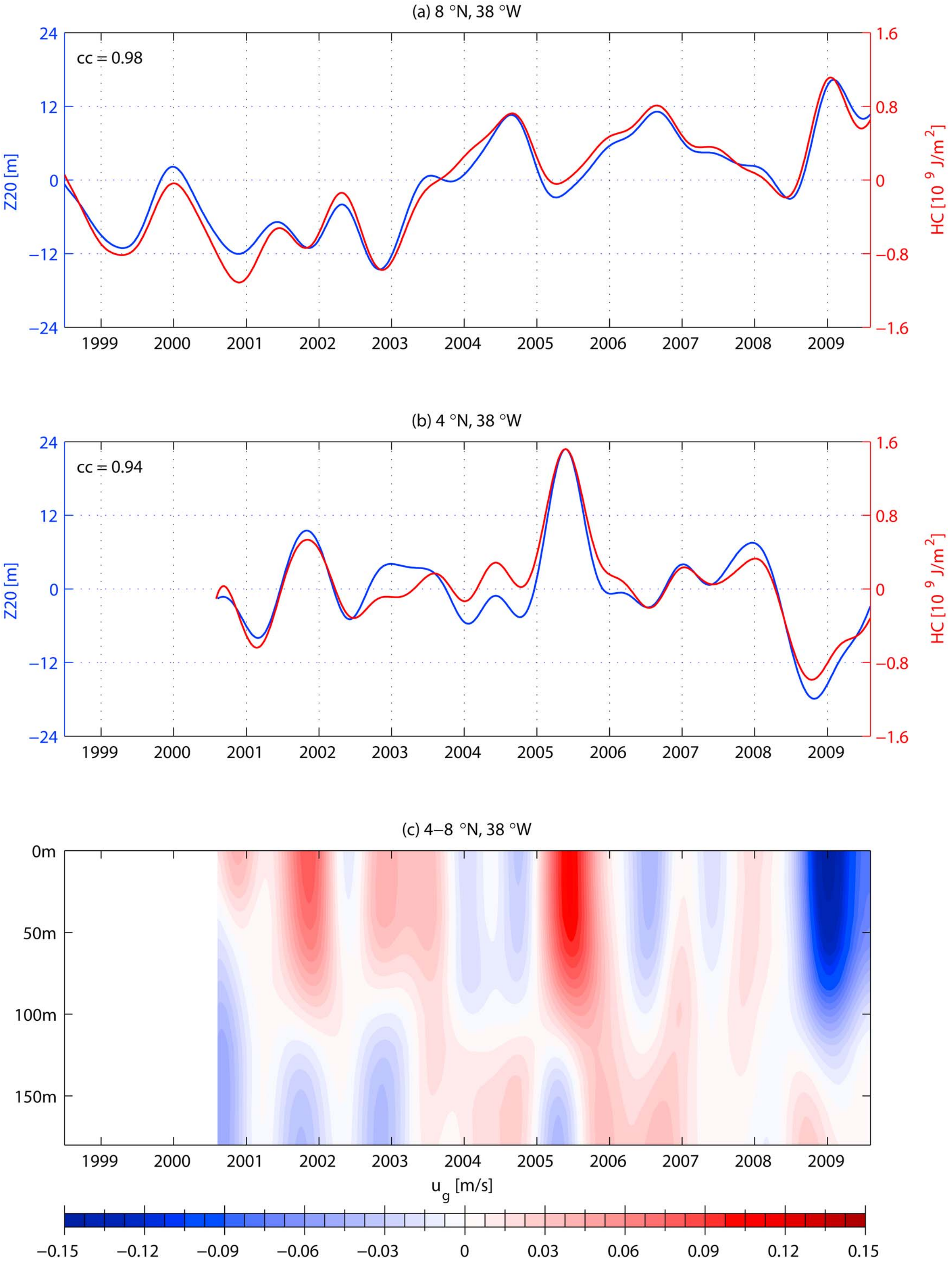

Figure 12. Interannual anomalies of 20°C-isotherm depth (blue) and upper 180m-heat content (red) at (a) 8°N and (b) 4°N, 38°W; the respective correlation coefficient is annotated. (c) Interannual anomalies of geostrophic velocity between 4°–8°N, 38°W.

to boreal summer/fall data a larger fraction of particles would be carried eastward by the seasonally intensified NECC. Figure 13 illustrates where particles within the NECC end up: After 10 days, most particles are still close to the release site but tend to spread eastward. The eastward advection within the NECC is further observable after 100 days, although there are now also indications for a northwestward pathway which is even more pronounced after one year (i.e., particles get sidetracked into the NEC). At that stage, other major concentration sites can be found consistent with advection

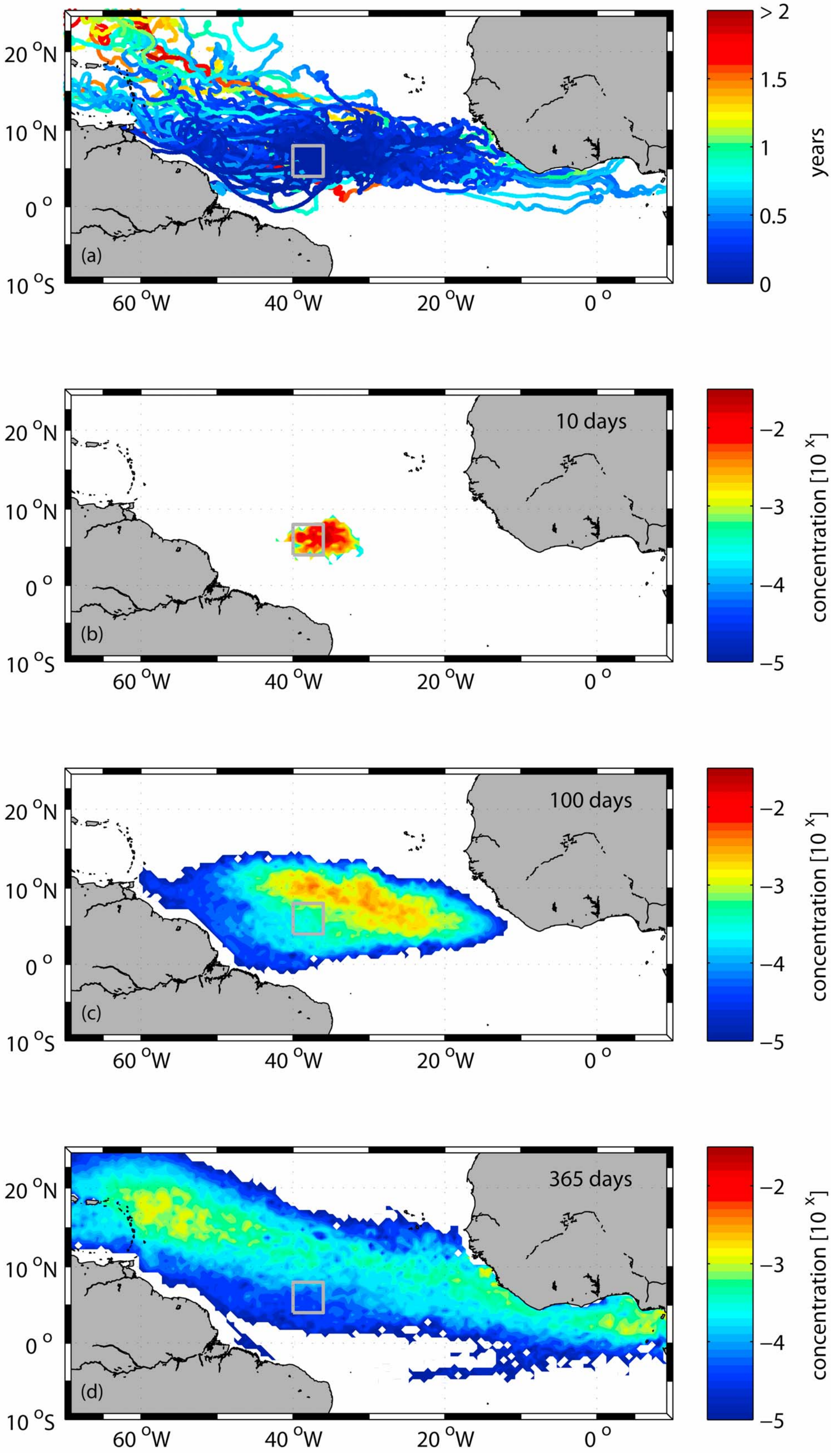

Figure 13. Lagrangian simulation: (a) drifter trajectories after passing 6°N, 38°W; (b–d) simulation of the evolution of a tracer released around 6°N, 38°W after 10 (Figure 13b), 100 (Figure 13c), and 365 days (Figure 13d), where 1 was the original concentration (i.e., all of the tracer in one bin). Release site is marked by gray box.

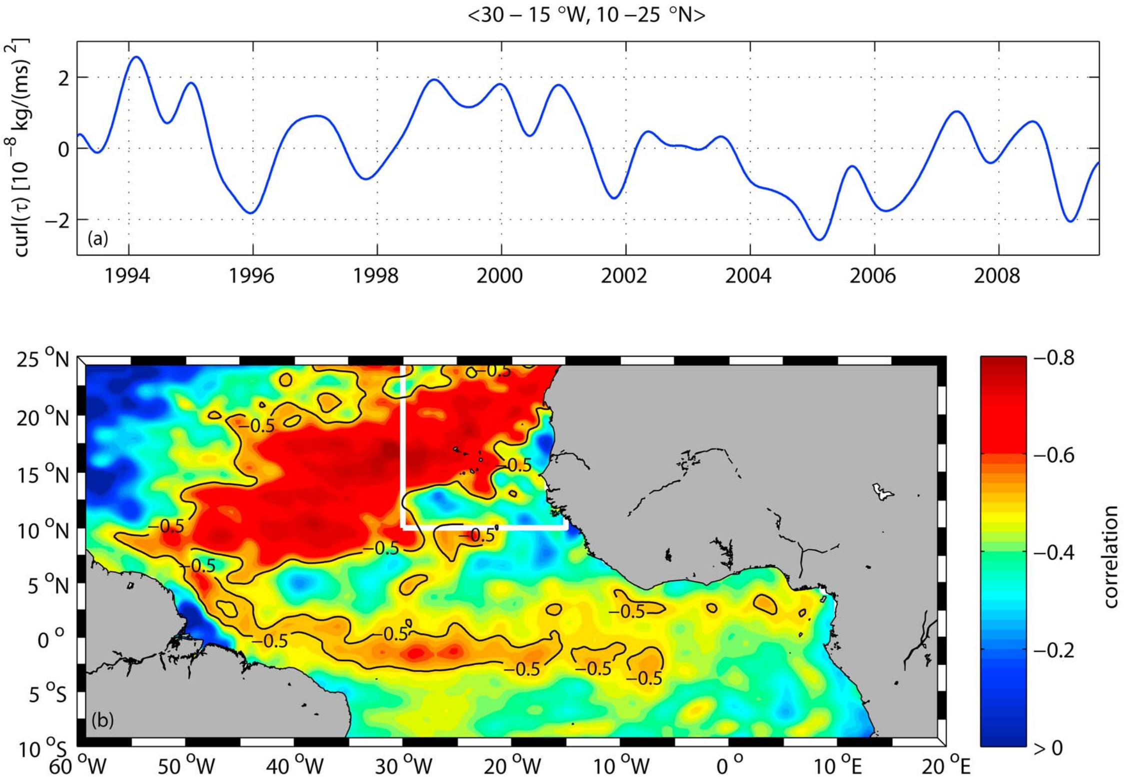

Figure 14. (a) Time series of interannual wind stress curl anomalies averaged over 10°–25°N, 30°–15°W. (b) Correlation of the time series shown in Figure 14a with interannual SSH anomalies in the tropical Atlantic; values not significant at 95% significance level are set to zero and white lines mark wind box.

along the African coast and the northern Gulf of Guinea. This simulation indicates overall that, for example, near-surface temperature anomalies advected within the NECC can contribute to anomalous SSTs in the northern hemisphere if horizontal SST gradients are non-zero where NECC variability is strong.

4. Discussion and Conclusion

[34] In this study, we have investigated the interannual variability of the NECC and its relation to the tropical Atlantic climate modes. It is widely accepted that the eastward NECC is a wind-driven, geostrophic current. Its interannual variability was quantified using a synthesis product of the surface geostrophic circulation that utilizes surface drifters, winds, and altimetry.

[35] Analyzing the interannual NECC variability in terms of a first CEOF mode revealed pronounced latitudinal displacements, variations in current strength, as well as prevailing northwestward propagation that is most pronounced northward of about 6°N. A Radon transform analysis indicated that the zonal propagation characteristics are consistent with long Rossby waves; the importance of these waves for NECC dynamics has already been recognized [e.g., *Garzoli and Katz*, 1983; *Korotaev and Chepurin*, 1992]. To trace the origin of this westward propagation, we performed a correlation analysis between interannual anomalies of wind stress curl and SSH. Results suggest that alongshore winds in the northeastern tropical Atlantic generate Rossby waves which propagate westward from the eastern boundary (cf. Section 3.2; Figure 14). Large correlations were also found along the western boundary and the equator which might be indicative of wave reflection processes, but we were not able to corroborate this. Note additionally that the wind time series shown in Figure 14a bears some resemblance to the 8°N-time series of interannual 20°C-isotherm depth and heat content anomalies (cf. Figure 12a), with correlation coefficients between them of $cc = -0.53$ and $cc = -0.60$ (both significant at 95% level), respectively.

[36] The analysis by *Garzoli and Katz* [1983] indicated that both Rossby waves from the eastern basin and local wind stress contribute to the seasonal variability of the thermocline depth. NECC composites for tropical Atlantic extreme events showed wind stress curl anomalies opposite in sign prevailing north and south of the maximum velocity fluctuations (cf. Figure 11), suggesting that similar dynamics are involved on interannual and seasonal timescales. On the other hand, *Yang and Joyce* [2006] hypothesized a leading role of equatorial wind stress forcing for seasonal variations of the Atlantic NECC since its southern flank at about 3°N is partially located in the equatorial waveguide. Our results suggest that such a mechanism might also act on longer interannual timescales. Indeed, regression of interannual NECC variations onto surface winds and SST revealed patterns reminiscent of the two dominant tropical Atlantic climate modes (cf. Figure 10), which have been shown to interact through wind-forced equatorial waves and their boundary reflections [*Foltz and McPhaden*, 2010]. Here, the proposed link between these modes was further supported by the finding of extreme meridional- and zonal-mode events of opposite sign in the

same year (cf. Figure 9b) as well as consistent NECC composites for warm phases of the meridional mode and cold phases of the zonal mode (cf. Figures 11b and 11c). Note that despite the known close relation between the NECC and the ITCZ [e.g., *Garzoli and Richardson*, 1989; *Garzoli*, 1992; *Korotaev and Chepurin*, 1992; *Fonseca et al.*, 2004] a comparable regression analysis based on our ITCZ index (cf. Figure 9b) solely resulted in a meridional-mode-like pattern (not shown). That is, an index based on the NECC, with its southern flank partially located in the equatorial waveguide, also takes equatorial dynamics into account and supports the proposed link between the two tropical Atlantic climate modes.

[37] *Joyce et al.* [2004] concluded that interannual cross-equatorial winds are positively correlated with heat content changes in the southern boundary region of the western NECC but not to its north. This is also in agreement with our observations along 38°W (cf. Figure 12) which showed interannual heat content anomalies at 4°N and 8°N to be unrelated, with two striking fluctuations at the southern site during 2005 and 2008/2009. The respective subsurface geostrophic velocities also indicated large anomalies in these time periods implying changes in NECC advection. Consistent with recent studies [*Foltz and McPhaden*, 2006; *Foltz et al.*, 2012], both 2005 and 2009 were found to be strong Atlantic meridional mode events (cf. Figure 9b). A clear relationship between this mode and changes in zonal NECC transport was noted by *Joyce et al.* [2004] based on both subsurface temperature observations and a numerical model hindcast.

[38] Our Lagrangian simulation revealed that a significant fraction of particles released within the NECC around 6°N, 38°W end up near the African coast (cf. Figure 13) and the mean distribution of tropical Atlantic surface currents indicated that the NECC appears to be part of the cyclonic circulation associated with the Guinea Dome (cf. Figure 3a). Recent model studies have proposed a link between the interannual variability of the Guinea Dome and the Atlantic meridional mode involving a negative feedback mechanism [*Doi et al.*, 2009, 2010]. Conversely, an observational analysis of the role of mixed layer dynamics during the strong meridional mode event in 2009 suggested that there may be positive coupled feedbacks between Ekman pumping anomalies north of the equator and the cross-equatorial SST gradient anomaly [*Foltz et al.*, 2012]. Although the latter study found a rather small contribution of horizontal temperature advection to the anomalous cooling in the tropical North Atlantic, it may play an important role during certain time periods. Of course, the coupled dynamics might be different for individual events due to influences of other modes of variability like the NAO and Pacific ENSO [e.g., *Czaja et al.*, 2002; *Enfield and Mayer*, 1997].

[39] Concerning ENSO, the mechanism proposed by *Zhang and Busalacchi* [1999], which links off-equatorial warm anomalies propagating along the Pacific NECC path and the onset of the 1997–98 El Niño, seems to be rather unlikely in the case of the Atlantic zonal mode since after one year our Lagrangian simulation shows very low particle concentrations in the ATL3 region (cf. Figure 13d).

[40] In conclusion, this study indicated that the relation between interannual NECC variability and the two dominant tropical Atlantic climate modes can primarily be regarded as a response to changes in the wind field. A better understanding of how interannual current variations interact with the meridional and zonal modes might be crucial for potential predictability of rainfall fluctuations, as interannual-to-decadal SST variability is closely linked with wind and rainfall variations over wide areas of the tropical Atlantic [e.g., *Chang et al.*, 2006, and references therein].

[41] **Acknowledgments.** This research was carried out in part under the auspices of the Cooperative Institute for Marine and Atmospheric Studies (CIMAS), a Cooperative Institute of the University of Miami and the National Oceanic and Atmospheric Administration (NOAA), cooperative agreement NA17RJ1226. Additional support was provided by NOAA's Climate Program Office and NOAA's Atlantic Oceanographic and Meteorological Laboratory. NCEP Daily Global Analyses data are provided by the NOAA/OAR/ESRL PSD, Boulder, Colorado, USA, from their web site at http://www.esrl.noaa.gov/psd/. The altimeter products were produced by Ssalto/Duacs and distributed by AVISO, with support from CNES (http://www.aviso.oceanobs.com/duacs/). PIRATA data are provided by the TAO project office (http://www.pmel.noaa.gov/tao/data_deliv/deliv.html). The Lagrangian simulation presented in this study was developed from code created by Nikolai Maximenko (University of Hawaii). Discussions with Peter Brandt and comments from Renellys Perez, three anonymous reviewers as well as the responsible editor Frank Bryan led to significant improvements in the manuscript.

References

Antonov, J. I., D. Seidov, T. P. Boyer, R. A. Locarnini, A. V. Mishonov, H. E. Garcia, O. K. Baranova, M. M. Zweng, and D. R. Johnson (2010), *World Ocean Atlas 2009*, vol. 2, *Salinity*, *NOAA Atlas NESDIS*, vol. 69, edited by S. Levitus, NOAA, Silver Spring, Md.

Arhan, M., H. Mercier, B. Bourlès, and Y. Gouriou (1998), Hydrographic sections across the Atlantic at 7°30N and 4°30S, *Deep Sea Res., Part I*, *45*, 829–872.

Arnault, S., B. Bourlès, Y. Gouriou, and R. Chuchla (1999), Intercomparison of the upper layer circulation of the western equatorial Atlantic Ocean: In situ and satellite data, *J. Geophys. Res.*, *104*, 21,171–21,194.

Artamonov, Y. V. (2006), Seasonal variability of geostrophic currents in the Atlantic Ocean according to the altimetry data, *Phys. Oceanogr.*, *16*, 177–187.

Atlas, R., R. N. Hoffman, J. Ardizzone, S. M. Leidner, J. C. Jusem, D. K. Smith, and D. Gombos (2011), A cross-calibrated, multiplatform ocean surface wind velocity product for meteorological and oceanographic applications, *Bull. Am. Meteorol. Soc.*, *92*, 157–174, doi:10.1175/2010BAMS2946.1.

Barber, C. B., D. P. Dobkin, and H. Huhdanpaa (1996), The Quickhull algorithm for convex hulls, *ACM Trans. Math. Software*, *22*, 469–483, doi:10.1145/235815.235821.

Barnett, T. P. (1983), Interaction of the monsoon and Pacific trade wind system at interannual time scales. Part I: The equatorial zone, *Mon. Weather Rev.*, *111*, 756–773.

Bourlès, B., Y. Gouriou, and R. Chuchla (1999), On the circulation in the upper layer of the western equatorial Atlantic, *J. Geophys. Res.*, *104*, 21,151–21,170.

Bourlès, B., et al. (2008), The PIRATA program: History, accomplishments, and future directions, *Bull. Am. Meteorol. Soc.*, *89*, 1111–1125, doi:10.1175/2008BAMS2462.1.

Brandt, P., G. Caniaux, B. Bourlès, A. Lazar, M. Dengler, A. Funk, V. Hormann, H. Giordani, and F. Marin (2011), Equatorial upper-ocean dynamics and their interaction with the West African monsoon, *Atmos. Sci. Lett.*, *12*, 24–30, doi:10.1002/asl.287.

Chang, P., L. Ji, and H. Li (1997), A decadal climate variation in the tropical Atlantic Ocean from thermodynamic air-sea interactions, *Nature*, *385*, 516–518.

Chang, P., et al. (2006), Climate fluctuations of tropical coupled systems—The role of ocean dynamics, *J. Clim.*, *19*, 5122–5174.

Chelton, D. B., and M. G. Schlax (1996), Global observations of oceanic Rossby waves, *Science*, *272*, 234–238.

Chelton, D. B., R. A. DeSzoeke, M. G. Schlax, K. E. Naggar, and N. Siwertz (1998), Geographical variability of the first baroclinic Rossby radius of deformation, *J. Phys. Oceanogr.*, *28*, 433–460.

Czaja, A., P. van der Vaart, and J. Marshall (2002), A diagnostic study of the role of remote forcing in tropical Atlantic variability, *J. Clim.*, *15*, 3280–3290.

Deans, S. R. (1983), *The Radon Transform and Some of its Applications*, John Wiley, Hoboken, N. J.

Didden, N., and F. Schott (1992), Seasonal variations in the western tropical Atlantic: Surface circulation from Geosat altimetry and WOCE model results, *J. Geophys. Res.*, *97*, 3529–3541.

Doi, T., T. Tozuka, and T. Yamagata (2009), Interannual variability of the Guinea Dome and its possible link with the Atlantic meridional mode, *Clim. Dyn.*, *33*, 985–998, doi:10.1007/s00382-009-0574-z.

Doi, T., T. Tozuka, and T. Yamagata (2010), The Atlantic meridional mode and its coupled variability with the Guinea Dome, *J. Clim.*, *23*, 455–475, doi:10.1175/2009JCLI3198.1.

Enfield, D. B., and D. A. Mayer (1997), Tropical Atlantic sea surface temperature variability and its relation to El Niño–Southern Oscillation, *J. Geophys. Res.*, *102*, 929–945.

Fairall, C. W., E. F. Bradley, J. E. Hare, A. A. Grachev, and J. B. Edson (2003), Bulk parameterization of air-sea fluxes: Updates and verification for the COARE algorithm, *J. Clim.*, *16*, 571–591.

Foltz, G. R., and M. J. McPhaden (2006), Unusually warm sea surface temperatures in the tropical North Atlantic during 2005, *Geophys. Res. Lett.*, *33*, L19703, doi:10.1029/2006GL027394.

Foltz, G. R., and M. J. McPhaden (2010), Interaction between the Atlantic meridional and Niño modes, *Geophys. Res. Lett.*, *37*, L18604, doi:10.1029/2010GL044001.

Foltz, G. R., M. J. McPhaden, and R. Lumpkin (2012), A strong Atlantic meridional mode event in 2009: The role of mixed layer dynamics, *J. Clim.*, *25*, 363–380, doi:10.1175/JCLI-D-11-00150.1.

Fonseca, C. A., G. J. Goni, W. E. Johns, and J. D. Campos (2004), Investigation of the North Brazil Current retroflection and North Equatorial Countercurrent variability, *Geophys. Res. Lett.*, *31*, L21304, doi:10.1029/2004GL020054.

Fratantoni, D. M., W. E. Johns, T. L. Townsend, and H. E. Hurlburt (2000), Low-latitude circulation and mass transport pathways in a model of the tropical Atlantic Ocean, *J. Phys. Oceanogr.*, *30*, 1944–1966.

Garzoli, S. L. (1992), The Atlantic North Equatorial Countercurrent: Models and observations, *J. Geophys. Res.*, *97*, 17,931–17,946.

Garzoli, S. L., and E. J. Katz (1983), The forced annual reversal of the Atlantic North Equatorial Countercurrent, *J. Phys. Oceanogr.*, *13*, 2082–2090.

Garzoli, S., and P. L. Richardson (1989), Low-frequency meandering of the Atlantic North Equatorial Countercurrent, *J. Geophys. Res.*, *94*, 2079–2090.

Góes, M., and I. Wainer (2003), Equatorial currents transport changes for extreme warm and cold events in the Atlantic Ocean, *Geophys. Res. Lett.*, *30*(5), 8006, doi:10.1029/2002GL015707.

Hormann, V., and P. Brandt (2007), Atlantic Equatorial Undercurrent and associated cold tongue variability, *J. Geophys. Res.*, *112*, C06017, doi:10.1029/2006JC003931.

Hormann, V., and P. Brandt (2009), Upper equatorial Atlantic variability during 2002 and 2005 associated with equatorial Kelvin waves, *J. Geophys. Res.*, *114*, C03007, doi:10.1029/2008JC005101.

Jochum, M., and P. Malanotte-Rizzoli (2001), Influence of the meridional overturning circulation on tropical-subtropical pathways, *J. Phys. Oceanogr.*, *31*, 1313–1323.

Jochum, M., and P. Malanotte-Rizzoli (2003), On the generation of North Brazil Current rings, *J. Mar. Res.*, *61*, 147–173.

Johnson, G. C., B. M. Sloyan, W. S. Kessler, and K. E. McTaggart (2002), Direct measurements of upper ocean currents and water properties across the tropical Pacific during the 1990s, *Prog. Oceangr.*, *52*, 31–61.

Johnston, T. M. S., and M. A. Merrifield (2000), Interannual geostrophic current anomalies in the near-equatorial western Pacific, *J. Phys. Oceanogr.*, *30*, 3–14.

Joyce, T. M., C. Frankignoul, J. Yang, and H. E. Phillips (2004), Ocean response and feedback to the SST dipole in the tropical Atlantic, *J. Phys. Oceanogr.*, *34*, 2525–2540.

Katz, E. J. (1993), An interannual study of the Atlantic North Equatorial Countercurrent, *J. Phys. Oceanogr.*, *23*, 116–123.

Keenlyside, N. S., and M. Latif (2007), Understanding equatorial Atlantic interannual variability, *J. Clim.*, *20*, 131–142, doi:10.1175/JCLI3992.1.

Korotaev, G. K., and G. A. Chepurin (1992), The mechanisms for seasonal restructuring of long current fields in the north tropical Atlantic Ocean, in *Investigations of the Tropical Atlantic Ocean*, edited by V. N. Eremeev, pp. 109–122, VSP Int., Utrecht, Netherlands.

Lagerloef, G. S. E., G. T. Mitchum, R. B. Lukas, and P. P. Niiler (1999), Tropical Pacific near-surface currents estimated from altimeter, wind, and drifter data, *J. Geophys. Res.*, *104*, 23,313–23,326.

Le Traon, P. Y., F. Nadal, and N. Ducet (1998), An improved mapping method of multi-satellite altimeter data, *J. Atmos. Oceanic Technol.*, *15*, 522–534.

Locarnini, R. A., A. V. Mishonov, J. I. Antonov, T. P. Boyer, H. E. Garcia, O. K. Baranova, M. M. Zweng, and D. R. Johnson (2010), *World Ocean Atlas 2009*, vol. 1, *Temperature*, *NOAA Atlas NESDIS*, vol. 68, edited by S. Levitus, NOAA, Silver Spring, Md.

Lumpkin, R., and Z. Garraffo (2005), Evaluating the decomposition of tropical Atlantic drifter observations, *J. Atmos. Oceanic Technol.*, *22*, 1403–1415.

Lumpkin, R., and S. L. Garzoli (2005), Near-surface circulation in the tropical Atlantic Ocean, *Deep Sea Res., Part I*, *52*, 495–518.

Maharaj, A. M., N. J. Holbrook, and P. Cipollini (2009), Multiple westward propagating signals in South Pacific sea level anomalies, *J. Geophys. Res.*, *114*, C12016, doi:10.1029/2008JC004799.

Marin, F., G. Caniaux, B. Bourlès, H. Giordani, Y. Gouriou, and E. Key (2009), Why were sea surface temperatures so different in the eastern equatorial Atlantic in June 2005 and 2006?, *J. Phys. Oceanogr.*, *39*, 1416–1431, doi:10.1175/2008JPO4030.1.

Maximenko, N. A., J. Hafner, and P. Niiler (2012), Pathways of marine debris derived from trajectories of Lagrangian drifters, *Mar. Pollut. Bull.*, *65*, 51–62, doi:10.1016/j.marpolbul.2011.04.016.

Niiler, P. P. (2001), The world ocean surface circulation, in *Ocean Circulation and Climate*, *Int. Geophys. Ser.*, vol. 77, edited by G. Siedler, J. Church, and J. Gould, pp. 193–204, Academic, New York.

Niiler, P. P., N. A. Maximenko, G. G. Panteleev, T. Yamagata, and D. Olson (2003), Near-surface dynamical structure of the Kuroshio extension, *J. Geophys. Res.*, *108*(C6), 3193, doi:10.1029/2002JC001461.

Polonsky, A. B., and Y. V. Artamonov (1997), North Equatorial Countercurrent in the tropical Atlantic: Multi-jet structure and seasonal variability, *Ocean Dyn.*, *49*, 477–495.

Ralph, E. A., and P. P. Niiler (1999), Wind-driven currents in the tropical Pacific, *J. Phys. Oceanogr.*, *29*, 2121–2129.

Reynolds, R. W., N. A. Rayner, T. M. Smith, D. C. Stokes, and W. Wang (2002), An improved in situ and satellite SST analysis for climate, *J. Clim.*, *15*, 1609–1625.

Richardson, P. L., and G. Reverdin (1987), Seasonal cycle of velocity in the Atlantic North Equatorial Countercurrent as measured by surface drifters, current meters, and ship drifts, *J. Geophys. Res.*, *92*, 3691–3708.

Servain, J. (1991), Simple climatic indices for the tropical Atlantic Ocean and some applications, *J. Geophys. Res.*, *96*, 15,137–15,146.

Servain, J., I. Wainer, J. P. McCreary Jr., and A. Dessier (1999), Relationship between the equatorial and meridional modes of climate variability in the tropical Atlantic, *Geophys. Res. Lett.*, *26*, 485–488.

Stramma, L., S. Hüttl, and J. Schafstall (2005), Water masses and currents in the upper tropical northeast Atlantic off northwest Africa, *J. Geophys. Res.*, *110*, C12006, doi:10.1029/2005JC002939.

Stramma, L., P. Brandt, J. Schafstall, F. Schott, J. Fischer, and A. Körtzinger (2008), Oxygen minimum zone in the North Atlantic south and east of the Cape Verde Islands, *J. Geophys. Res.*, *113*, C04014, doi:10.1029/2007JC004369.

Urbano, D. F., M. Jochum, and I. C. A. da Silveira (2006), Rediscovering the second core of the Atlantic NECC, *Ocean Modell.*, *12*, 1–15, doi:10.1016/j.ocemod.2005.04.003.

Urbano, D. F., R. A. F. De Almeida, and P. Nobre (2008), Equatorial Undercurrent and North Equatorial Countercurrent at 38°W: A new perspective from direct velocity data, *J. Geophys. Res.*, *113*, C04041, doi:10.1029/2007JC004215.

Yang, J., and T. M. Joyce (2006), Local and equatorial forcing of seasonal variations of the North Equatorial Countercurrent in the Atlantic Ocean, *J. Phys. Oceanogr.*, *36*, 238–254.

Zebiak, S. E. (1993), Air-sea interaction in the equatorial Atlantic region, *J. Clim.*, *6*, 1567–1586.

Zhang, R.-H., and A. J. Busalacchi (1999), A possible link between off-equatorial warm anomalies propagating along the NECC path and the onset of the 1997–98 El Niño, *Geophys. Res. Lett.*, *26*, 2873–2876.